Orientation dependence of even-order harmonics generation in biased bilayer graphene

Yajuan Ren,[1,2,3] Lei Jia,[4] Yupeng Zhang,[1,2,3] Zhe Zhang,[1,2,3] Shan Xue,[2] Shengjun Yue,[1,2,3,*] and Hongchuan Du[1,2,3,†]

[1]*Frontiers Science Center for Rare Isotopes, Lanzhou University, Lanzhou 730000, China*

[2]*School of Nuclear Science and Technology, Lanzhou University, Lanzhou 730000, China*

[3]*Key Laboratory of Special Function Materials and Structure Design, Ministry of Education, Lanzhou University, Lanzhou 730000, China*

[4]*Key Laboratory for Magnetism and Magnetic Materials of the Ministry of Education, Lanzhou University, Lanzhou 730000, China*

(Received 2 June 2022; accepted 14 September 2022; published 30 September 2022)

We theoretically study the orientation dependence of even-order harmonics in biased bilayer graphene (BLG) by numerically solving the semiconductor Bloch equations in the velocity gauge. It is shown that the yield of even-order harmonics has a perfect periodicity of 60° with the rotation of the crystal orientation. The even-harmonic intensity reaches the maximum when the laser field is polarized along with the nearest-neighbor atom. By investigating the crystal orientation dependence for the parallel and perpendicular components of even harmonics, it is found that the Berry curvature plays an insignificant role in the even-harmonic generation of biased BLG. Further analysis reveals that the asymmetric electron density between in-plane adjacent atoms caused by polarization is responsible for the generation of even harmonics in biased BLG. Additionally, we study the ellipticity dependence of even harmonics in biased BLG when the elliptical principal axis of the laser pulse is along with the in-plane nearest-neighbor atoms. As expected, the yield of even harmonics decreases with the ellipticity. Our findings give access to understanding deeply the mechanism of the orientation dependence of even harmonics in biased BLG.

DOI: 10.1103/PhysRevA.106.033123

I. INTRODUCTION

High-order harmonic generation (HHG), an important and nonperturbative optical phenomenon in strong-field physics, has been investigated as a means for providing new extreme ultraviolet and soft X-ray light sources. Despite the extensive investigations of gas HHG [1–5], the low atomic density leads to the low conversion efficiency of HHG. This limits the development and application of gas HHG. Thanks to the advance of midinfrared laser technology, solid HHG has become a hot topic in strong-field and condensed matter physics so far. It not only provides a new approach to attosecond photonics [6,7], but also brings a powerful tool for the detection of structures and ultrafast dynamic processes in condensed matters [8,9].

Compared with HHG in gases, solid HHG presents more abundant physical phenomena and more complex characteristics, such as multiplateau structures [10–12], linear scaling of cutoff energy with laser field amplitude [13], anomalous ellipticity dependence of HHG [14–18], and so on. The spatial symmetry of translation, rotation, inversion, and reflection of the periodic lattice structure strongly influence HHG in solids. As is known, the harmonic intensity is sensitive to the crystal orientation [16,19,20]. This orientation dependence of HHG was demonstrated to be related to many ultrafast processes in crystals [21–28]. For example, it was found in the monolayer MoS_2 [16] that the even harmonics are predominately polarized perpendicular to the polarization of the laser field and the intensity reaches the maximum when the laser field is perpendicular to the mirror plane. This is attributed to the anomalous current induced by the Berry curvature. However, for ZnO crystal [29], even harmonics are only generated if the laser polarization is along the mirror plane. This indicates that the orientation-dependent higher-order harmonic spectra contain the structure information of crystals and can be applied to probe crystal band structure [30].

Two-dimensional (2D) materials exhibit unique electronic properties [31–34] and symmetry properties [35] that have a significant impact on the process of HHG. Graphene, a 2D hexagonal lattice of carbon atoms, its electronic band structure has led to massless Dirac fermion physics [36] and an anomalous quantum Hall effect [37]. Recently, it was shown that the valley polarization can be achieved by using two counterrotating circularly polarized laser pulses [38,39]. With one more graphene layer added, bilayer graphene has an entirely different but equally interesting band structure. Compared with monolayer graphene, the electronic states of biased bilayer graphene (BLG) are considerably richer [40] and the band gap is widely tunable [41]. Both theoretical and experimental studies [41–44] showed that the band gap of BLG can be controlled by an applied electric field which is perpendicular to the graphene plane [41–43]. This makes BLG the only known semiconductor with a tunable energy gap up to 250 meV and opens the way for developing applications like nanoelectronic and nanophotonic devices [44], thermoelectric devices [45], photodetectors [46], high-frequency transistors [47], and so on. As is well known, the gapped BLG can generate even-order harmonics because of symmetry breaking [42,43]. However, the generation mechanism of

*yuesj@lzu.edu.cn
†duhch@lzu.edu.cn

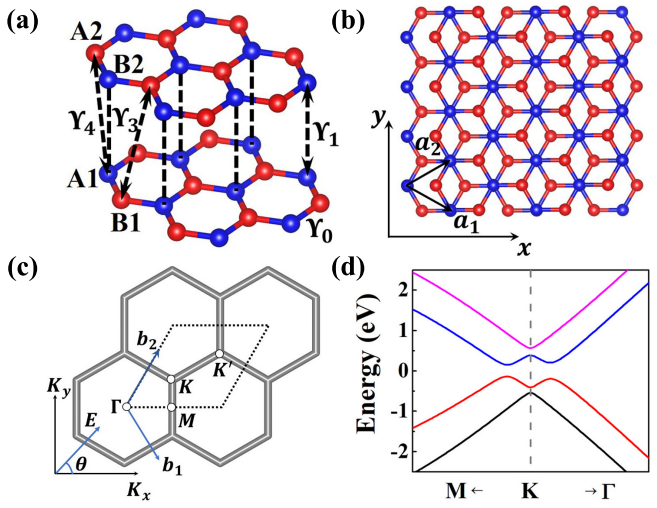

FIG. 1. (a) Crystal structure of the BLG (AB stacked) with the Slonczewski-Weiss-McClure parameters. (b) Top view of BLG (AB stacked). (c) Brillouin zone. (d) Band structure of the biased BLG with $\Delta = 0.4$ eV.

even-order harmonics is yet to be discussed. Moreover, the research on the orientation dependence of even-order harmonics in biased BLG is still lacking.

In this work, we explore the orientation dependence of even-order harmonics in biased BLG. Differing from the even-order harmonic generation caused by the Berry curvature [16,24,48–50], we find that the even harmonics are mainly polarized along with the polarization of the laser field. In addition, the maximum harmonic yields occur only when the laser field is polarized along with the in-plane nearest-neighbor atoms. Further investigation demonstrates that the interlayer coupling can lead to the polarization of in-plane adjacent atoms due to the existence of interlayer voltage in biased BLG. The radiation of even-order harmonics is the consequence of the asymmetrical electron density of neighboring atoms. An intuitive physical model is established to understand the orientation dependence of even-order harmonics. Finally, we study the ellipticity dependence of even harmonics.

This paper is organized as follows. In Sec. II, we introduce the theoretical method. In Sec. III, the orientation dependence of even harmonics in biased BLG is studied in detail. The orientation dependence of high harmonics is presented in Sec. III A. In Sec. III B, we investigate the generation mechanism of even-order harmonics and explain the orientation dependence of even-order harmonics by a molecular model extracted from the biased BLG. Section III C focuses on the ellipticity dependence of even harmonics. Finally, the summary is given in Sec. IV.

II. THEORETICAL MODEL

The BLG is a system between graphene and bulk graphite. The crystal structure of AB stacking is shown in Fig. 1(a), where sites A1 and B1 denote the two inequivalent atoms on the lower unit cell. A2 and B2 are the counterparts on the upper cell. The layers are arranged as follows: the atom B2 is on the top of the atom A1. These two atomic sites are referred to as "dimer" sites because the electron orbitals on them are coupled together by a relatively strong interlayer coupling. Atoms B1 and A2 are located, respectively, at the center of the hexagonal lattice on the other layer and are referred to as "nondimer" sites. The commensurate top view is illustrated in Fig. 1(b). $\mathbf{a}_1 = (\frac{\sqrt{3}a}{2}, \frac{a}{2})$ and $\mathbf{a}_2 = (\frac{\sqrt{3}a}{2}, -\frac{a}{2})$ are the two primitive lattice vectors with the lattice constant a =2.46 Å. The Brillouin zone (BZ) is displayed in Fig. 1(c). $\mathbf{b}_1 = (\frac{2\pi}{\sqrt{3}a}, \frac{2\pi}{a})$ and $\mathbf{b}_2 = (\frac{2\pi}{\sqrt{3}a}, -\frac{2\pi}{a})$ are the reciprocal lattice vectors. $\mathbf{K} = (\frac{2\pi}{\sqrt{3}a}, \frac{2\pi}{3a})$ and $\mathbf{K}' = (\frac{4\pi}{\sqrt{3}a}, \frac{4\pi}{3a})$ represent two inequivalent high-symmetry points referred to as Dirac points. $\mathbf{E}$ is the polarization direction of the laser electric field and θ is the angle with the K_x axis. We sample the Brillouin zone shown as the dashed lines in Fig. 1(c) using a grid with 1000×1000 points in the calculations. This processing is equivalent to sampling the first Brillouin zone.

TABLE I. Tight-binding parameters used for biased BLG in units of eV.

γ_0	γ_1	γ_3	γ_4	Δ'
3.16	0.381	0.38	0.14	0.022

The electronic structure of biased BLG is modeled by the tight-binding approximation with the Slonczewski-Weiss-McClure (SWMc) parametrization [34,40]. The Hamiltonian in reciprocal space reads

$$H(\mathbf{k}) = \begin{pmatrix} -\Delta - \frac{\Delta'}{2} & -\gamma_0 f(\mathbf{k}) & \gamma_4 f(\mathbf{k}) & -\gamma_3 f^*(\mathbf{k}) \\ -\gamma_0 f^*(\mathbf{k}) & -\Delta + \frac{\Delta'}{2} & \gamma_1 & \gamma_4 f(\mathbf{k}) \\ \gamma_4 f^*(\mathbf{k}) & \gamma_1 & \Delta + \frac{\Delta'}{2} & -\gamma_0 f(\mathbf{k}) \\ -\gamma_3 f(\mathbf{k}) & \gamma_4 f^*(\mathbf{k}) & -\gamma_0 f^*(\mathbf{k}) & \Delta - \frac{\Delta'}{2} \end{pmatrix}, \quad (1)$$

where the function $f(\mathbf{k})$ is given by

$$f(\mathbf{k}) = \exp\left(i\frac{ak_x}{\sqrt{3}}\right) + 2\exp\left(-i\frac{ak_x}{2\sqrt{3}}\right)\cos\left(\frac{ak_y}{2}\right). \quad (2)$$

Here, the effect of the bias field is incorporated by shifting the onsite potentials of the two layers by $\pm\Delta$ with $\Delta = 0.4$ eV. γ_0, γ_1, γ_3, and γ_4 are illustrated in Fig. 1(a). γ_0 is the hopping parameter between in-plane nearest-neighbor atoms. γ_1 describes the interlayer coupling between pairs of orbitals on the dimer sites A1 and B2. γ_3 describes the interlayer coupling between pairs of orbitals on the nondimer sites A2 and B1. γ_4 describes the interlayer coupling between dimer and nondimer orbitals A2 and A1 or B2 and B1. Δ' is the energy difference between dimer and nondimer sites [51]. In Table I, we list the SWMc parameters used in our simulation and these parameters can be found in Ref. [34]. The eigenvalue $E_n^{\mathbf{k}}$ and eigenfunction $u_n^{\mathbf{k}}$ are obtained by diagonalizing the Hamiltonian. Here, $u_n^{\mathbf{k}}$ is the periodic part of Bloch function $\Psi_n^{\mathbf{k}} = u_n^{\mathbf{k}} e^{i\mathbf{k}\cdot\mathbf{r}}$. Figure 1(d) shows the band structure of the biased BLG with $\Delta = 0.4$ eV.

To describe the interaction of strong-laser fields and biased BLG, we solve the velocity gauge semiconductor Bloch equations (SBEs) in the Bloch representation. In general, the

SBEs of the velocity gauge require more bands to guarantee converged results [52–54]. However, for bilayer graphene of the tight-binding model with four bands since the basis set is complete in this condition, the SBEs of the velocity gauge in the tight-binding model can obtain reliable results [24,55–57]. The SBEs are used as follows (atomic units are used throughout unless otherwise stated):

$$\frac{\partial \rho^{\mathbf{k}}_{mn}(t)}{\partial t} = i\left[E^{\mathbf{k}}_m - E^{\mathbf{k}}_n + \frac{i(1-\delta_{mn})}{T_2}\right]\rho^{\mathbf{k}}_{mn}(t) - i\mathbf{A}(t)\cdot\sum_l \left[\mathbf{P}^{\mathbf{k}}_{nl}\rho^{\mathbf{k}}_{ml}(t) - \mathbf{P}^{\mathbf{k}}_{lm}\rho^{\mathbf{k}}_{ln}(t)\right], \quad (3)$$

with the density matrix element $\rho^{\mathbf{k}}_{mn}(t)$, defined as $\rho_{mn} = a^*_m a_n$. a_m and a_n are the expanded coefficients of the time-dependent wave function under the Bloch representation. The matrix element of the momentum operator $\mathbf{P}^{\mathbf{k}}_{nl}$ can be obtained by

$$\mathbf{P}^{\mathbf{k}}_{nm} = \langle u_{n\mathbf{k}}|\frac{\partial H(\mathbf{k})}{\partial \mathbf{k}}|u_{m\mathbf{k}}\rangle. \quad (4)$$

The driving laser field is

$$\mathbf{E}(t) = \frac{E_0}{\sqrt{1+\varepsilon^2}} f(t)[\cos(\omega_0 t)\hat{\mathbf{e}}_x + \varepsilon \sin(\omega_0 t)\hat{\mathbf{e}}_y], \quad (5)$$

where the vector potential is calculated by $\mathbf{A}(t) = -\int_{-\infty}^{t}\mathbf{E}(t)dt$. E_0 and ω_0 are the amplitude and the angular frequency of a 3000 nm laser field with the intensity $3.15\times10^{11}\,\mathrm{W/cm^2}$. The laser field has a $\cos^2$ envelop with a total duration of 20 optical cycles. ε is the ellipticity. The polarization of the laser field transitions from linear to circular when the ellipticity varies from $\varepsilon = 0$ to $\varepsilon = 1$. The dephasing time is set as $T_2 = 5$ fs. Decoherence describes the phenomenon that the coherence of a quantum system decays as the interactions within the system that increase with time. In HHG of solids, the dephasing time involves the interaction between the electron under consideration and its environment: other electrons, ions, phonons, impurities of the system. The clear high-order harmonic spectrum observed in experiments can be reproduced theoretically when taking the dephasing time into account [52]. However, the dephasing time has not been determined in solid harmonic generation so far. Different dephasing times are used in different literature. Here, the dephasing time $T_2 = 5$ fs is applied to obtain clear harmonics and does not affect the result of the orientation dependence.

In our calculations, we use the classical fourth-order Runge-Kutta method to solve the SBEs. The time step is 0.4137 a.u. The convergence of the time step and space step in k space was tested. The electric current induced by the laser field reads

$$\mathbf{J}(t) = \sum_{m,n}\int_{\mathrm{BZ}}\mathbf{P}^{\mathbf{k}}_{mn}\rho^{\mathbf{k}}_{mn}(t)d^2\mathbf{k}. \quad (6)$$

We decompose the current in the directions parallel and perpendicular to the laser polarization directions

$$\mathbf{J}(t) = J_{\parallel}(t)\mathbf{e}_{\parallel} + J_{\perp}(t)\mathbf{e}_{\perp}. \quad (7)$$

$\mathbf{e}_{\parallel}$ and $\mathbf{e}_{\perp}$ are unit vectors corresponding to the directions parallel and perpendicular to the laser polarization. The harmonic spectrum can be obtained by the modulus square of the Fourier transform of the electric current

$$I(\omega) = I_{\parallel}(\omega) + I_{\perp}(\omega),$$
$$I_{\parallel}(\omega) \propto |\mathrm{FT}[J_{\parallel}(t)]|^2,$$
$$I_{\perp}(\omega) \propto |\mathrm{FT}[J_{\perp}(t)]|^2. \quad (8)$$

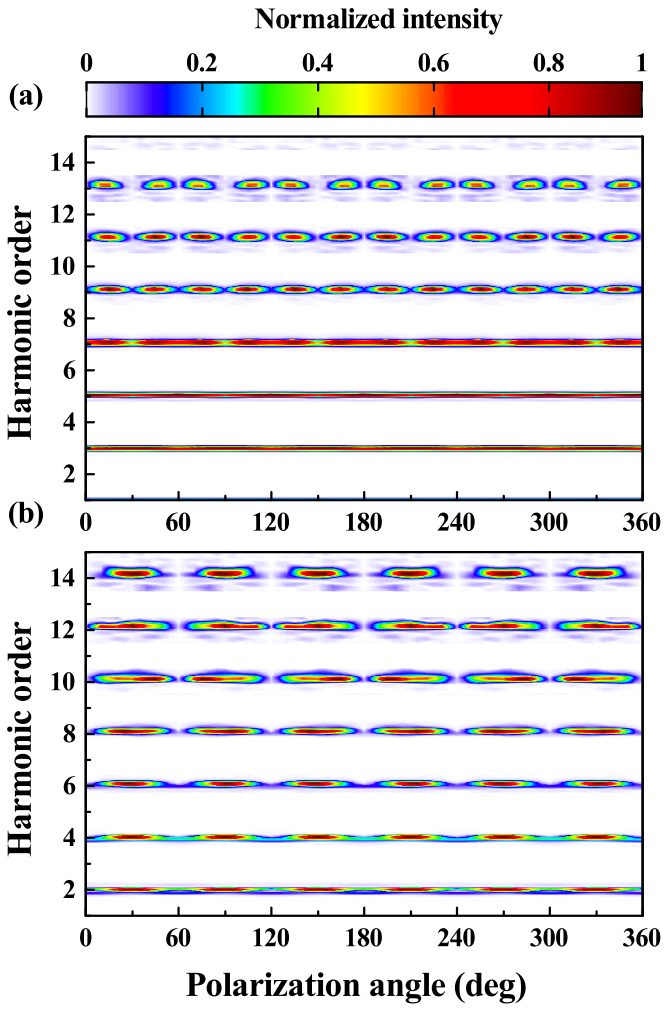

FIG. 2. Orientation dependence of (a) odd-order harmonics and (b) even-order harmonics resulting from the linearly polarized laser pulse with intensity $3.15\times10^{11}\,\mathrm{W/cm^2}$ and wavelength 3000 nm.

III. RESULTS AND DISCUSSIONS

A. Orientation dependence of harmonics

We first calculate the orientation dependence of the harmonics generated from the biased BLG in the driving of the linearly polarized field. As shown in Fig. 1(c), the angle θ between the laser polarization and the K_x axis in the BZ is defined as the polarization angle. When the polarization direction of the laser field is along with Γ–M in the reciprocal space, the laser field is polarized along the y axis in the real space. In our calculation, the polarization angle varies from 0° to 360° with an interval of 5°. Because of the symmetry breaking caused by the biased electric field, both odd-order and even-order harmonics are produced, see Fig. 3(c).

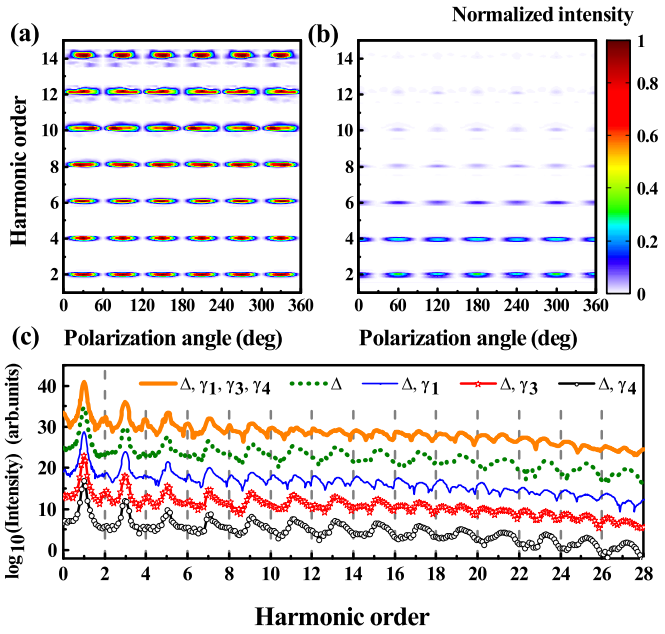

FIG. 3. Orientation dependence of the (a) parallel and (b) perpendicular components of even-order harmonics. (c) Harmonic spectra at different interlayer parameters with the laser polarization direction located at 0°. The various harmonic spectra are shown with different curves: thick orange solid lines (bias voltage Δ, γ_1, γ_3, γ_4); olive dotted lines (bias voltage Δ); thin blue solid lines (bias voltage Δ, γ_1); red lines connected by stars (bias voltage Δ, γ_3); and black lines connected by circles (bias voltage Δ, γ_4).

Figure 2 presents the orientation dependence of odd-order [Fig. 2(a)] and even-order harmonics [Fig. 2(b)]. For clarity, the harmonic intensity is normalized to the maximum harmonic intensity of all scanned angles. The same normalization is used in the latter harmonic orientation dependence. Here, we focus on the harmonics with orders above sixth that are contributed to by the interband currents. As shown, the odd-order and even-order harmonics exhibit significantly different orientation dependence. Although both of them have a 60° periodicity, the odd-order harmonics show a distinct double-peak structure in every period. Both peaks locate at about $15° + 60°n$ and $45° + 60°n$ (n is an integer). However, for even-order harmonics, there is only one peak in every period, which appears around $30° + 60°n$ (n is an integer). The orientation dependence of odd-order harmonics was discussed in Ref. [27]. In the following, we aim at studying the orientation dependence of the even-order harmonics.

B. Interpretation of the orientation dependence of even-order harmonics

For exploring the mechanism of even-order harmonic generation, we decompose the current into the components parallel and perpendicular to the polarized direction of the laser field by Eq. (8). The harmonic spectra are obtained according to Eq. (7). Figures 3(a) and 3(b) show the orientation dependence of the parallel and perpendicular components, respectively. By comparison, it can be seen that the parallel current component mainly contributes to the generation of even-order harmonics, while the contribution of the vertical current component can be ignored. It means the Berry curvature does not dominate the even-order harmonic generation since the polarization of even-order harmonics induced by the Berry curvature is orthogonal to the polarization direction of the laser field [24]. We further study the influence of the interlayer parameters on the generation of even-order harmonics. The results are shown in Fig. 3(c). Both odd-order and even-order harmonics are observed in the total harmonic spectrum, labeled as thick orange solid lines in Fig. 3(c). The total harmonic spectrum is calculated by including all coupling parameters in the presence of the bias voltage. Olive dotted lines represent the case only in the presence of the bias voltage without interlayer coupling effects, in which the even-order harmonics vanish. This indicates that the interlayer coupling is essential for the generation of even-order harmonics.

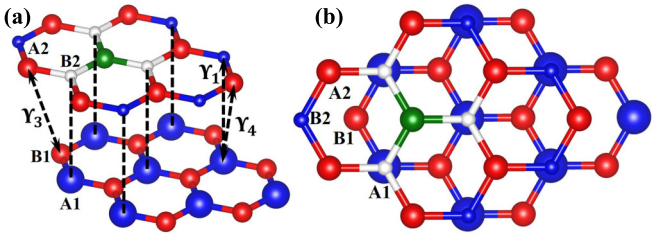

FIG. 4. (a) Schematic structure of the Y-type model. The size of an atom reflects the electron density. (b) Top view of the model.

The question now is which coupling parameter dominates the generation of even-order harmonics. To answer this question, as shown in Fig. 3(c), we use individual parameters γ_1, γ_3, and γ_4 to calculate the harmonic spectra of the biased BLG. To distinguish the curves clearly, all lines (except for black lines connected by circles) are shifted up by factors of 6 (red lines connected by stars), 12 (thin blue solid lines), 18 (olive dotted lines), and 24 (thick orange solid lines). The following conditions are found. (i) As shown in the black lines connected by circles (only with γ_4), there exist only the odd-order harmonics. (ii) The even-order harmonics above order 16 can be generated in the case of considering γ_3, see the red lines connected by stars. (iii) When γ_1 is considered, clear and strong even-order harmonics can be observed in the entire harmonic spectrum, see the thin blue solid line. Therefore, the interlayer coupling parameters γ_1 are responsible for the generation of even-order harmonics for orders 6 to 14.

We next investigate how γ_1 contributes to the even-harmonic generation in the biased BLG from a symmetry perspective. We choose four atoms A1, B1, A2, and B2 in Fig. 1(a) to illustrate the impact of γ_1 on the symmetry of the structure. When the biased voltage Δ exists, the polarization between atoms A1 and B2 caused by γ_1 will lead to the asymmetric electron density distribution between atoms A1 and B2. This results in the unequal electron density between atoms A2 and B2 (atoms A1 and B1). A structural schematic diagram in Fig. 4 is built to intuitively understand such unequal distribution of electron density. The electron density is mapped to the size of atoms. The upper and lower layers of the crystal structure can be reproduced by translating

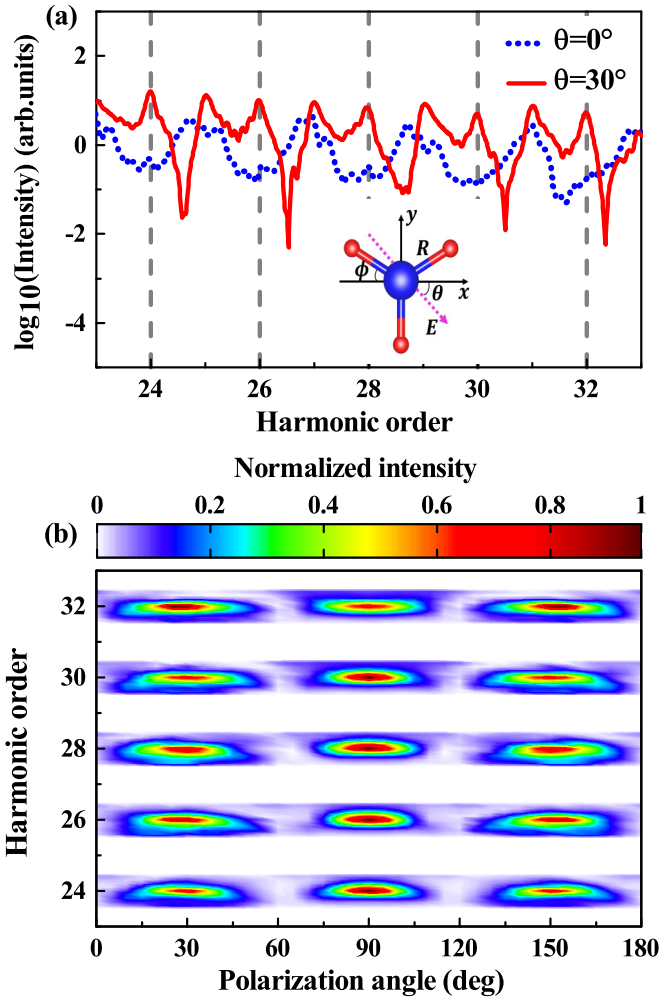

FIG. 5. (a) High-harmonic spectra of the Y-type model at two different polarization angles driven by an 800-nm laser field with the intensity 3.5×10^{14} W/cm^2. The angle θ is defined as the angle between the laser polarization direction and the x axis. The sketch in the middle part of (a) illustrates the structure of the Y-type modeling molecules. The magenta arrow is the polarization direction of the laser field. ϕ is the angle between the model bond and the x axis. R is the internuclear distance. (b) Orientation dependence of the corresponding even-order harmonics.

the Y-shaped structure, which is highlighted with green and white balls. Based on this, we concentrate on the HHG from the Y-shaped structure. According to the selection rule of HHG [58], the even-order harmonics can be generated from the Y-shaped structure in the driving of linearly polarized lasers. This verifies that the even-order harmonics are induced by the structural asymmetries caused by γ_1.

To consolidate the physical picture, we develop a molecular model to investigate the orientation dependence of even-order harmonics generated from the Y-shaped structure. The Y-shaped structure processes the 120° rotation symmetry. The model is constructed using three A atoms with the same charge and one B atom with a larger charge, i.e., BA_3. The B atom is located at the crossroads of the Y type, and the three A atoms are located at the three endpoints of the Y as shown in the inset of Fig. 5(a). The time-dependent Schrödinger equation (TDSE) in the length gauge reads

$$i\frac{\partial}{\partial t}\psi(\mathbf{r},t) = \left[-\frac{\nabla_{\mathbf{r}}^2}{2} + V(\mathbf{r}) + \mathbf{r}\cdot\mathbf{E}(t)\right]\psi(\mathbf{r},t). \quad (9)$$

In this model, the movement of the electron is limited to 2D space with the coordinate $\mathbf{r}$. The interaction potential between the electron and ions $V(\mathbf{r})$ is constituted by four terms:

$$V(\mathbf{r}) = -\frac{Z_A}{\sqrt{(\mathbf{r}-\mathbf{r}_1)^2+\alpha}} - \frac{Z_A}{\sqrt{(\mathbf{r}-\mathbf{r}_2)^2+\alpha}} - \frac{Z_A}{\sqrt{(\mathbf{r}-\mathbf{r}_3)^2+\alpha}} - \frac{Z_B}{\sqrt{\mathbf{r}^2+\alpha}}. \quad (10)$$

Here, $\alpha = 2.0$ a.u. is the softcore parameter. Z_A and Z_B correspond to the charge of the atoms A and B. We obtain the corresponding eigenstates by diagonalizing the tight-binding Hamiltonian of the biased bilayer graphene in the real space. Considering that the electrons at the top of the valence band mainly contribute to the harmonic generation, we calculate the electron population of different cells and the electron population ratio of two unequal carbon atoms in the same cell using the wave function of the highest occupied state in the valence band. It is found that the electron population ratios in cells with high electron population are all close to the value 1.5. Therefore, we choose $Z_A = 1$ and $Z_B = 1.5$. Note that, in a certain range, Z_B does not affect our conclusions. $\mathbf{r}_1 = (R\cos\phi)\mathbf{e_x} + (R\sin\phi)\mathbf{e_y}$, $\mathbf{r}_2 = (-R\cos\phi)\mathbf{e_x} + (R\sin\phi)\mathbf{e_y}$, and $\mathbf{r}_3 = -R\mathbf{e_y}$ are the coordinates of the three A atoms, where $R = 4.0$ a.u. is the internuclear distance between atoms A and B. $\phi = 30°$ is the angle between the molecular bond and the x axis, as shown in the inset of Fig. 5(a). The electric field $\mathbf{E}(t)$ is given by Eq. (5) with $\varepsilon = 0$. The wavelength is 800 nm and the intensity is 3.5×10^{14} W/cm^2. The envelope $f(t)$ of the electric field is trapezoidal with two-cycle linear ramps in ten optical cycles.

The 2D TDSE is numerically solved using the Crank-Nicolson method [59] with a time step $\Delta t = 0.1$ a.u. The space box size is $L_x \times L_y = 200 \times 200$ a.u. with grids 4000×4000. For each time step, the mask function along the x axis is $F(x) = \cos^{\frac{1}{8}}[\pi(|x| - x_0)/2(L_x - x_0)]$ for $x_0 \leqslant |x| \leqslant L_x$ and $F(x) = 1$ for $|x| \leqslant x_0$ with $x_0 = 4/9L_x$. In the y direction, a similar treatment is applied with $y_0 = 4/9L_y$. Such a treatment can avoid the reflections of wave functions at the boundary. Once the time-dependent wave function is obtained, the dipole acceleration $\mathbf{a}(t)$ can be calculated via the Ehrenfest theorem [60]

$$\mathbf{a}(t) = \langle\psi(\mathbf{r},t)|\partial_{\mathbf{r}}(V(r) + \mathbf{r}\cdot\mathbf{E}(t))|\psi(\mathbf{r},t)\rangle. \quad (11)$$

Then the harmonic spectrum can be given by the modulus square of the Fourier transform of the dipole acceleration.

Figure 5(a) presents the harmonic spectra at two polarization angles of the laser field. Compared to the case of $\theta = 0°$, the intensity of the even-order harmonics is significantly enhanced in the case of $\theta = 30°$. Further, the orientation dependence of the even-order harmonics is shown in Fig. 5(b). Here, we show the results of 0°–180°, which are the same as those of 180°–360°. Clearly, the harmonic intensity has a periodicity of 60° and reaches a maximum at $\theta = 30°, 90°, 150°$, which are directions along the model bonds. Also, we de-

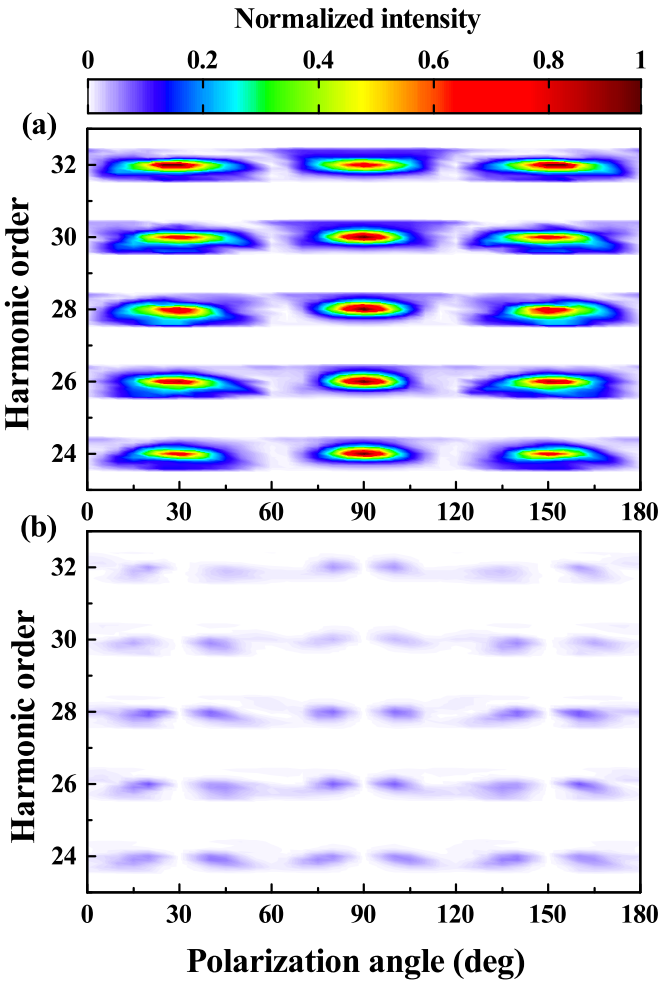

FIG. 6. Orientation dependence of the (a) parallel and (b) perpendicular components of even-order harmonics generated from the Y-shaped model. The laser parameters are same as Fig. 5.

compose the dipole acceleration using the same procedure as in biased BLG. It is found that the parallel component of the dipole acceleration dominates the generation of even-order harmonics, see Fig. 6. These results match well with those of the biased BLG. It means that the asymmetry of the electron density distribution between two atoms (A1B1 or A2B2) is responsible for the even-harmonic generation in biased BLG. For AA stacking bilayer graphene, the second layer is placed on top of the first layer. Therefore, the electron density is equally transferred between two layers when the perpendicular electric field exists, which does not lead to the asymmetric distribution of electron density between in-plane adjacent atoms; thus no even harmonics are generated.

C. Ellipticity dependence of harmonic yield

In this section, we study the ellipticity dependence of harmonic yield in the biased BLG. Since the component amplitude of the laser field along the C–C bond decreases with the laser ellipticity, it leads to the reduction of the coupling between the two atoms (with asymmetrical electron density distribution). Together with the above truth, we conclude that the yield of even harmonics in the biased BLG should

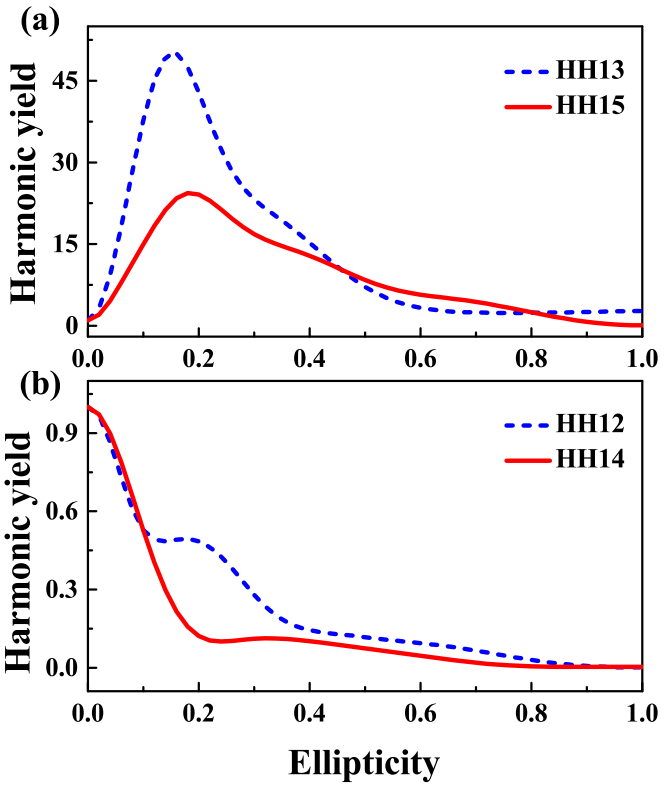

FIG. 7. (a) Ellipticity dependence of HH13 (blue dashed line) and HH15 (red line). (b) Ellipticity dependence of HH12 (blue dashed line) and HH14 (red line). The harmonic yield is normalized to the harmonic yield of $\varepsilon = 0$. The amplitude and angular frequency of the laser field are the same as Fig. 2.

decrease with the increasing ellipticity of the driving pulse when the elliptical principal axis of the laser field is along the C–C direction in one plane. Here, the yield of the nth harmonic is evaluated via

$$\mathbf{I}_n = \int_{(n-0.5)\omega_0}^{(n+0.5)\omega_0} \mathbf{I}_\omega d\omega. \tag{12}$$

Figures 7(a) and 7(b) show the yields of odd-order and even-order harmonics as a function of ellipticity. The harmonics above 0.4 eV follow the same law because they are both dominated by interband mechanisms. Therefore, we take the results of HH12, HH13, HH14, and HH15 as examples. As shown in Fig. 7(a), the ellipticity dependence of HH13 and HH15 is anomalous, namely, the harmonic yield reaches the maximum value at ellipticity around $\varepsilon = 0.2$, which was studied in monolayer graphene [15]. Based on the previous studies [18,61], we believe that the electrons and holes excited near the K or K′ point may form an approximately closed trajectory in real space when $\varepsilon = 0.2$, which may result in the anomalous ellipticity dependence of odd harmonics in biased bilayer graphene. As expected, for the even harmonics HH12 and HH14, the harmonic yields decrease with the ellipticity, see Fig. 7(b).

IV. CONCLUSION

In summary, we investigate the orientation dependence of even-order harmonics in biased BLG. It is found that, unlike

the even-order harmonics contributed to by the Berry curvature, the even-order harmonics in biased BLG are mainly dominated by the electric current parallel to the polarized direction of the laser field. Further studies show that, in the presence of bias voltages, the interlayer coupling parameter γ_1 leads to the inhomogeneous distribution of electron density between adjacent carbon atoms in the same layer of BLG, causing the generation of even-order harmonics. The good agreement of the orientation dependence of even-order harmonics between a Y-shaped structural model (with the asymmetric charge distribution) and biased BLG confirms our conclusion. In addition, we study the ellipticity dependence of the even-order harmonics in biased BLG. As expected, the yield of even-order harmonics decreases with the ellipticity of the laser when the elliptical principal axis of the laser is along with the C–C bond in the layer. In the future, we expect the ellipticity dependence of even-order harmonics in biased BLG can be observed in the experiments.

Finally, we discuss the difference in even harmonic generation mechanisms between biased BLG and monolayer MoS_2. For biased BLG, the π covalent bonds formed by $2p_z$ orbitals of the two inequivalent C atoms mainly contribute to the energy band structure near the Fermi surface. So the inhomogeneous distribution of the electron density between the two inequivalent C atoms dominates the generation of even-order harmonics in biased BLG. However, for MoS_2, the d_{z^2}, d_{xy}, and $d_{x^2-y^2}$ orbits of the Mo atom mainly contribute to the energy band structure near the Fermi surface. Therefore, the contribution of the inhomogeneous distribution of electron density between the Mo atom and S atom can be ignored. The Berry curvature dominates the even-order harmonics generation in MoS_2.

ACKNOWLEDGMENTS

This work was supported by the National Natural Science Foundation of China (Grants No. 11874030, No. 11904146, No. 12064023, No. 12204209, and No. 12274188), the Natural Science Foundation of Gansu Province (Grant No. 20JR5RA209), and the Scientific Research Program of the Higher Education Institutions of Gansu Province of China (Grant No. 2020A-125).

[1] A. McPherson, G. Gibson, H. Jara, U. Johann, T. S. Luk, I. A. McIntyre, K. Boyer, and C. K. Rhodes, Studies of multiphoton production of vacuum-ultraviolet radiation in the rare gases, J. Opt. Soc. Am. B **4**, 595 (1987).

[2] M. Ferray, A. L'Huillier, X. F. Li, L. A. Lompre, G. Mainfray, and C. Manus, Multiple-harmonic conversion of 1064 nm radiation in rare gases, J. Phys. B: At. Mol. Opt. Phys. **21**, L31 (1988).

[3] C. Winterfeldt, C. Spielmann, and G. Gerber, Colloquium: Optimal control of high-harmonic generation, Rev. Mod. Phys. **80**, 117 (2008).

[4] D. Popmintchev, C. Hernández-García, F. Dollar, C. Mancuso, J. A. Pérez-Hernández, M. C. Chen, A. Hankla, X. H. Gao, B. Shim, A. L. Gaeta, M. Tarazkar, D. A. Romanov, R. J. Levis, J. A. Gaffney, M. Foord, S. B. Libby, A. Jaron-Becker, A. Becker, L. Plaja, M. M. Murnane *et al.*, Ultraviolet surprise: Efficient soft X-ray high-harmonic generation in multiply ionized plasmas, Science **350**, 1225 (2015).

[5] P. M. Kraus, B. Mignolet, D. Baykusheva, A. Rupenyan, L. Horný, E. F. Penka, G. Grassi, O. I. Tolstikhin, J. Schneider, F. Jensen, L. B. Madsen, A. D. Bandrauk, F. Remacle, and H. J. Wörner, Measurement and laser control of attosecond charge migration in ionized iodoacetylene, Science **350**, 790 (2015).

[6] T. T. Luu, M. Garg, S. Y. Kruchinin, A. Moulet, M. T. Hassan, and E. Goulielmakis, Extreme ultraviolet high-harmonic spectroscopy of solids, Nature (London) **521**, 498 (2015).

[7] M. Garg, M. Zhan, T. T. Luu, H. Lakhotia, T. Klostermann, A. Guggenmos, and E. Goulielmakis, Multi-petahertz electronic metrology, Nature (London) **538**, 359 (2016).

[8] G. Vampa, T. J. Hammond, N. Thiré, B. E. Schmidt, F. Légaré, C. R. McDonald, T. Brabec, D. D. Klug, and P. B. Corkum, All-Optical Reconstruction of Crystal Band Structure, Phys. Rev. Lett. **115**, 193603 (2015).

[9] N. Tancogne-Dejean, O. D. Mücke, F. X. Kärtner, and A. Rubio, Impact of the Electronic Band Structure in High-Harmonic Generation Spectra of Solids, Phys. Rev. Lett. **118**, 087403 (2017).

[10] M. Wu, S. Ghimire, D. A. Reis, K. J. Schafer, and M. B. Gaarde, High-harmonic generation from Bloch electrons in solids, Phys. Rev. A **91**, 043839 (2015).

[11] G. Ndabashimiye, S. Ghimire, M. Wu, D. A. Browne, K. J. Schafer, M. B. Gaarde, and D. A. Reis, Solid-state harmonics beyond the atomic limit, Nature (London) **534**, 520 (2016).

[12] T.-Y. Du, Z. Guan, X.-X. Zhou, and X.-B. Bian, Enhanced high-order harmonic generation from periodic potentials in inhomogeneous laser fields, Phys. Rev. A **94**, 023419 (2016).

[13] T. Higuchi, M. I. Stockman, and P. Hommelhoff, Strong-Field Perspective on High-Harmonic Radiation from Bulk Solids, Phys. Rev. Lett. **113**, 213901 (2014).

[14] C. Liu, Y. Zheng, Z. Zeng, and R. Li, Effect of elliptical polarization of driving field on high-order-harmonic generation in semiconductor ZnO, Phys. Rev. A **93**, 043806 (2016).

[15] N. Yoshikawa, T. Tamaya, and K. Tanaka, High-harmonic generation in graphene enhanced by elliptically polarized light excitation, Science **356**, 736 (2017).

[16] H. Liu, Y. Li, Y. S. You, S. Ghimire, T. F. Heinz, and D. A. Reis, High-harmonic generation from an atomically thin semiconductor, Nat. Phys. **13**, 262 (2017).

[17] N. Tancogne-Dejean, O. D. Mücke, F. X. Kärtner, and A. Rubio, Ellipticity dependence of high-harmonic generation in solids originating from coupled intraband and interband dynamics, Nat. Commun. **8**, 745 (2017).

[18] Y. Feng, S. Shi, J. Li, Y. Ren, X. Zhang, J. Chen, and H. Du, Semiclassical analysis of ellipticity dependence of harmonic yield in graphene, Phys. Rev. A **104**, 043525 (2021).

[19] S. Gholam-Mirzaei, J. Beetar, and M. Chini, High harmonic generation in ZnO with a high-power mid-IR OPA, Appl. Phys. Lett. **110**, 061101 (2017).

[20] Y. S. You, D. A. Reis, and S. Ghimire, Anisotropic high-harmonic generation in bulk crystals, Nat. Phys. **13**, 345 (2017).

[21] M. Wu, Y. You, S. Ghimire, D. A. Reis, D. A. Browne, K. J. Schafer, and M. B. Gaarde, Orientation dependence of temporal and spectral properties of high-order harmonics in solids, Phys. Rev. A **96**, 063412 (2017).

[22] S. Jiang, J. Chen, H. Wei, C. Yu, R. Lu, and C. D. Lin, Role of the Transition Dipole Amplitude and Phase on the Generation of Odd and Even High-Order Harmonics in Crystals, Phys. Rev. Lett. **120**, 253201 (2018).

[23] S. Jiang, S. Gholam-Mirzaei, E. Crites, J. E. Beetar, M. Singh, R. Lu, M. Chini, and C. Lin, Crystal symmetry and polarization of high-order harmonics in ZnO, J. Phys. B: At. Mol. Opt. Phys. **52**, 225601 (2019).

[24] C. Liu, Y. Zheng, Z. Zeng, and R. Li, Polarization-resolved analysis of high-order harmonic generation in monolayer MoS_2, New J. Phys. **22**, 073046 (2020).

[25] L. Li, Y. Zhang, P. Lan, T. Huang, X. Zhu, C. Zhai, K. Yang, L. He, Q. Zhang, W. Cao, and P. Lu, Dynamic Core Polarization in High Harmonic Generation from Solids: The Example of MgO Crystals, Phys. Rev. Lett. **126**, 187401 (2021).

[26] Y. Zhang, L. Li, J. Li, T. Huang, P. Lan, and P. Lu, Orientation dependence of high-order harmonic generation in graphene, Phys. Rev. A **104**, 033110 (2021).

[27] M. S. Mrudul and G. Dixit, High-harmonic generation from monolayer and bilayer graphene, Phys. Rev. B **103**, 094308 (2021).

[28] R. Zuo, A. Trautmann, G. Wang, W.-R. Hannes, S. Yang, X. Song, T. Meier, M. Ciappina, H. T. Duc, and W. Yang, Neighboring atom collisions in solid-state high harmonic generation, Ultrafast Science **2021**1 (2021).

[29] S. Ghimire, A. D. DiChiara, E. Sistrunk, P. Agostini, L. F. DiMauro, and D. A. Reis, Observation of high-order harmonic generation in a bulk crystal, Nat. Phys. **7**, 138 (2011).

[30] C. Yu, S. Jiang, T. Wu, G. Yuan, Z. Wang, C. Jin, and R. Lu, Two-dimensional imaging of energy bands from crystal orientation dependent higher-order harmonic spectra in $h-$BN, Phys. Rev. B **98**, 085439 (2018).

[31] K. S. Novoselov, A. K. Geim, S. V. Morozov, D. Jiang, Y. Zhang, S. V. Dubonos, I. V. Grigorieva, and A. A. Firsov, Electric field effect in atomically thin carbon films, Science **306**, 666 (2004).

[32] K. S. Novoselov, D. Jiang, F. Schedin, T. Booth, V. Khotkevich, S. Morozov, and A. K. Geim, Two-dimensional atomic crystals, Proc. Natl. Acad. Sci. USA **102**, 10451 (2005).

[33] K. I. Bolotin, K. J. Sikes, Z. Jiang, M. Klima, G. Fudenberg, J. Hone, P. Kim, and H. Stormer, Ultrahigh electron mobility in suspended graphene, Solid State Commun. **146**, 351 (2008).

[34] E. McCann and M. Koshino, The electronic properties of bilayer graphene, Rep. Prog. Phys. **76**, 056503 (2013).

[35] A. Molina-Sánchez and L. Wirtz, Phonons in single-layer and few-layer MoS_2 and WS_2, Phys. Rev. B **84**, 155413 (2011).

[36] K. S. Novoselov, A. K. Geim, S. V. Morozov, D. Jiang, M. I. Katsnelson, I. Grigorieva, S. Dubonos, and A. Firsov, Two-dimensional gas of massless Dirac fermions in graphene, Nature (London) **438**, 197 (2005).

[37] E. McCann and V. I. Fal'ko, Landau-Level Degeneracy and Quantum Hall Effect in a Graphite Bilayer, Phys. Rev. Lett. **96**, 086805 (2006).

[38] M. Mrudul, Á. Jiménez-Galán, M. Ivanov, and G. Dixit, Light-induced valleytronics in pristine graphene, Optica **8**, 422 (2021).

[39] M. Mrudul and G. Dixit, Controlling valley-polarisation in graphene via tailored light pulses, J. Phys. B: At. Mol. Opt. Phys. **54**, 224001 (2021).

[40] L. M. Zhang, Z. Q. Li, D. N. Basov, M. M. Fogler, Z. Hao, and M. C. Martin, Determination of the electronic structure of bilayer graphene from infrared spectroscopy, Phys. Rev. B **78**, 235408 (2008).

[41] E. V. Castro, K. S. Novoselov, S. V. Morozov, N. M. R. Peres, J. M. B. Lopes dos Santos, J. Nilsson, F. Guinea, A. K. Geim, and A. H. Castro Neto, Biased Bilayer Graphene: Semiconductor with a Gap Tunable by the Electric Field Effect, Phys. Rev. Lett. **99**, 216802 (2007).

[42] E. McCann, Asymmetry gap in the electronic band structure of bilayer graphene, Phys. Rev. B **74**, 161403(R) (2006).

[43] K. F. Mak, C. H. Lui, J. Shan, and T. F. Heinz, Observation of an Electric-Field-Induced Band Gap in Bilayer Graphene by Infrared Spectroscopy, Phys. Rev. Lett. **102**, 256405 (2009).

[44] Y. Zhang, T.-T. Tang, C. Girit, Z. Hao, M. C. Martin, A. Zettl, M. F. Crommie, Y. R. Shen, and F. Wang, Direct observation of a widely tunable bandgap in bilayer graphene, Nature (London) **459**, 820 (2009).

[45] C. R. Wang, W. S. Lu, L. Hao, W. L. Lee, T. K. Lee, F. Lin, I. Chun Cheng, and J. Z. Chen, Enhanced Thermoelectric Power in Dual-Gated Bilayer Graphene, Phys. Rev. Lett. **107**, 186602 (2011).

[46] J. Yan, M.-H. Kim, J. A. Elle, A. B. Sushkov, G. S. Jenkins, H. M. Milchberg, M. S. Fuhrer, and H. D. Drew, Dual-gated bilayer graphene hot-electron bolometer, Nat. Nanotechnol. **7**, 472 (2012).

[47] F. Xia, D. B. Farmer, Y. Lin, and P. Avouris, Graphene field-effect transistors with high on/off current ratio and large transport band gap at room temperature, Nano Lett. **10**, 715 (2010).

[48] S. Jiang, H. Wei, J. Chen, C. Yu, R. Lu, and C. D. Lin, Effect of transition dipole phase on high-order-harmonic generation in solid materials, Phys. Rev. A **96**, 053850 (2017).

[49] T. T. Luu and H. J. Wörner, Measurement of the Berry curvature of solids using high-harmonic spectroscopy, Nat. Commun. **9**, 916 (2018).

[50] A. Bharti, M. S. Mrudul, and G. Dixit, High-harmonic spectroscopy of light-driven nonlinear anisotropic anomalous hall effect in a weyl semimetal, Phys. Rev. B **105**, 155140 (2022).

[51] M. Dresselhaus and G. Dresselhaus, Intercalation compounds of graphite, Adv. Phys. **30**, 139 (1981).

[52] G. Vampa, C. R. McDonald, G. Orlando, D. D. Klug, P. B. Corkum, and T. Brabec, Theoretical Analysis of High-Harmonic Generation in Solids, Phys. Rev. Lett. **113**, 073901 (2014).

[53] V. S. Yakovlev, S. Y. Kruchinin, T. Paasch-Colberg, M. I. Stockman, and F. Krausz, Ultrafast control of strong-field electron dynamics in solids, in *Ultrafast Dynamics Driven by Intense Light Pulses* (Springer, New York, 2016), pp. 295–315.

[54] L. Yue and M. B. Gaarde, Structure gauges and laser gauges for the semiconductor bloch equations in high-order harmonic generation in solids, Phys. Rev. A **101**, 053411 (2020).

[55] M. Du, C. Liu, Z. Zeng, and R. Li, High-order harmonic generation from twisted bilayer graphene driven by a midinfrared laser field, Phys. Rev. A **104**, 033113 (2021).

[56] J. Chen, C. Liu, Z. Zeng, and R. Li, Control of ultrafast photocurrent in twisted bilayer graphene by circularly polarized few-cycle lasers, Phys. Rev. B **105**, 014309 (2022).

[57] D. Kim, D. Shin, A. S. Landsman, D. E. Kim, and A. Chacón, Theory for all-optical responses in topological materials: the velocity gauge picture, arXiv:2105.12294 v1.

[58] N. Ben-Tal, N. Moiseyev, and A. Beswick, The effect of hamiltonian symmetry on generation of odd and even harmonics, J. Phys. B: At. Mol. Opt. Phys. **26**, 3017 (1993).

[59] M. Nurhuda and F. H. M. Faisal, Numerical solution of time-dependent schrödinger equation for multiphoton processes: A matrix iterative method, Phys. Rev. A **60**, 3125 (1999).

[60] P. Ehrenfest, Bemerkung über die angenäherte Gültigkeit der klassischen Mechanik innerhalb der Quantenmechanik, Z. Phys. **45**, 455 (1927).

[61] L. Yue and M. B. Gaarde, Expanded view of electron-hole recollisions in solid-state high-order harmonic generation: Full-brillouin-zone tunneling and imperfect recollisions, Phys. Rev. A **103**, 063105 (2021).